Innovative Magnetic Nanoparticles for PET/MRI Bimodal Imaging

Guillaume Thomas, Julien Boudon, Lionel Maurizi, Mathieu Moreau, Paul Walker, Isabelle Séverin, Alexandra Oudot, Christine Goze, Sophie Poty, Jean-Marc Vrigneaud, et al.

ACS OMEGA

Article

Cite This: ACS Omega 2019, 4, 2637−2648

http://pubs.acs.org/journal/acsodf

Innovative Magnetic Nanoparticles for PET/MRI Bimodal Imaging

Guillaume Thomas,[†,#] Julien Boudon,[†] Lionel Maurizi,[†] Mathieu Moreau,[‡] Paul Walker,[§] Isabelle Severin,[∥] Alexandra Oudot,[⊥] Christine Goze,[‡] Sophie Poty,[‡] Jean-Marc Vrigneaud,[⊥] Fréderic Demoisson,[†] Franck Denat,[‡] François Brunotte,[⊥] and Nadine Millot*[,†]

[†]ICB UMR 6303 CNRS-Université Bourgogne Franche-Comté, 21000 Dijon, France

[‡]ICMUB UMR 6302 CNRS-Université Bourgogne Franche-Comté, 21000 Dijon, France

[§]Département de Spectroscopie par Résonance Magnétique, CHU Dijon, 21000 Dijon, France

[∥]UBFC-AgrosupDijon-INSERM U 1231, 1 Esplanade Erasme, 21000 Dijon, France

[⊥]Plateforme d'Imagerie Préclinique, Service de Médecine Nucléaire, Centre Georges François Leclerc, 21000 Dijon, France

Supporting Information

ABSTRACT: Superparamagnetic iron oxide nanoparticles were developed as positron emission tomography (PET) and magnetic resonance imaging (MRI) bimodal imaging agents. These nanoparticles (NPs), with a specific nanoflower morphology, were first synthesized and simultaneously functionalized with 3,4-dihydroxy-L-phenylalanine (LDOPA) under continuous hydrothermal conditions. The resulting NPs exhibited a low hydrodynamic size of 90 ± 2 nm. The functional groups of LDOPA (−NH_2 and −COOH) were successfully used for the grafting of molecules of interest in a second step. The nanostructures were modified by poly(ethylene glycol) (PEG) and a new macrocyclic chelator MANOTA for further ^{64}Cu radiolabeling for PET imaging. The functionalized NPs showed promising bimodal (PET and MRI) imaging capability with high r_2 and r_2* (T_2 and T_2* relaxivities) values and good stability. They were mainly uptaken from liver and kidneys. No cytotoxicity effect was observed. These NPs appear as a good candidate for bimodal tracers in PET/MRI.

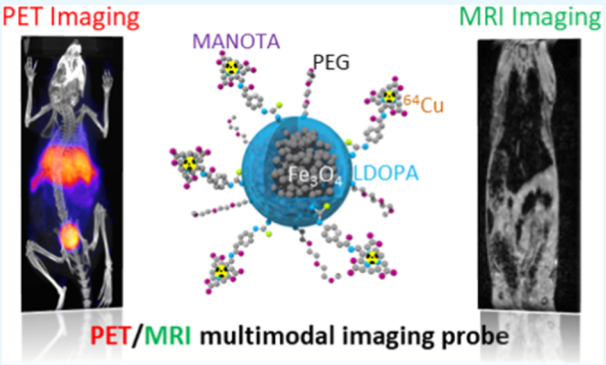

1. INTRODUCTION

Magnetic iron oxide NPs have received huge attention in biomedical applications such as magnetic resonance imaging (MRI),[1,2] hyperthermia,[3] and drug delivery.[4] In particular, superparamagnetic iron oxide nanoparticles (SPIONs) are widely used as in vivo transverse relaxation (T_2 and T_2*) contrast agents in molecular and cell imaging to differentiate diseased from healthy tissues.[5]

However, since each imaging modality possesses its own strengths and weaknesses, one single imaging technique is often not enough to evaluate the biological structure properties and information concerning a pathology or an injury with accuracy and in real time.[6] More particularly, MRI has low sensitivity and is not appropriate for molecular imaging.[5] To overcome these drawbacks, multimodal imaging approaches, combining MRI with a complementary imaging technique, such as positron emission tomography (PET), are very interesting. Indeed, such a strategy allows to apply an effective treatment as soon as possible. In one step, the mechanisms of pathologies are indicated. A rapid, specific, and appropriate treatment can be consequently applied on the patient.[7]

Magnetic iron oxide NPs are nowadays used as potential multimodal imaging probes[7−10] such as PET/MRI,[6] MRI/ultrasound (US),[11] MRI/computed tomography (CT),[12] or PET/near-infrared fluorescence/MRI.[13] It can be highly beneficial to combine PET with MRI. PET is highly sensitive and particularly well suited for molecular imaging.[5,7] The simultaneous use of MRI and PET imaging leads to high spatial resolution, high sensitivity, high technical maturity, and low radiation doses.[6,9] Thus, a radiolabeled MRI probe such as radiolabeled SPIONs may show great potential as an innovative, powerful, and promising tool to enhance the noninvasive diagnosis and treatment of patients.

Iron oxide NPs have been studied and modified to develop multifunctional contrast agents with high biocompatibility and stability over a wide range of pH.[2,13] They should satisfy several requirements such as a good long-term stability, a high efficiency for imaging or drug delivery, and nonspecific interactions between the NP surface and the biological media. Many strategies have been developed to improve these characteristics. They consist in the grafting of electrostatic and/or steric agents on the surface of the NPs.[14−23]

Received: November 25, 2018
Accepted: January 14, 2019
Published: February 5, 2019

DOI: 10.1021/acsomega.8b03283
ACS Omega 2019, 4, 2637−2648

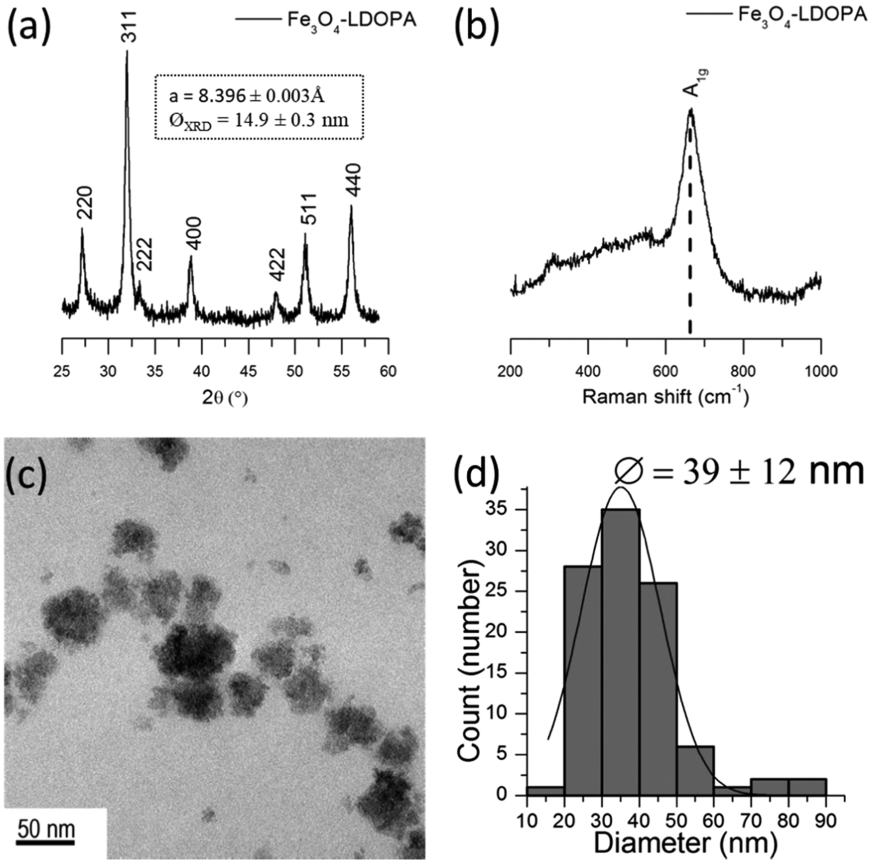

Figure 1. (a) XRD pattern, (b) Raman spectra, (c) transmission electron microscopy (TEM) image, and (d) TEM diameter distribution of Fe_3O_4−LDOPA NPs.

Some studies reported that catechol derivatives such as LDOPA,[24] dopamine,[25] and nitrodopamine[26] have a strong affinity to metal oxides and can be used as a platform to graft other molecules such as poly(ethylene glycol) (PEG) and acyclic chelators, owing to their multiple functional groups (−NH_2, −COOH, −OH).[22,27−29] Macrocyclic bifunctional chelating agents can also be advantageously used because they form more stable complexes with radiometals used for PET imaging, thus preventing transchelation or transmetallation phenomenon.[30] Different shapes and sizes of macrocycles are used to complex various metallic radioisotopes such as $^{64}Cu^{2+}$, $^{67/68}Ga^{3+}$, $^{111}In^{3+}$, etc. For examples, the most widely used macrocyclic derivatives are those of the 1,4,7,10-tetraazacyclododecane-1,4,7,10-tetraacetic acid and the one of 1,4,7-triazacyclononane-1,4,7-triacetic acid known as DOTA and NOTA respectively. However, only a few PET/MRI bimodal imaging contrast agents based on iron oxide NPs have been developed.[6,13,21,31−36] Patel et al. reported a PET/MRI imaging contrast agent using iron oxide NPs coated with DOTA to chelate Cu^{2+}.[6] Lee et al. developed a tumor-specific iron oxide probe for early clinical tumor detection using PET/MRI multimodal imaging.[34] More recently, Rosales et al. used a different strategy by developing functionalized bimodal PET/MRI NPs including molecules containing dithiocarbamate groups (sulfur derivatives of carbamate functions) aiming at the chelation of ^{64}Cu.[31] This radioactive isotope is a very good candidate for PET imaging owing to its 12.7 h half-life, which allows to record images and until 24 h after injection.[37−42]

In our study, we aimed to develop for the first time a dual PET/MRI imaging nanoprobe based on SPIONs initially synthesized and modified by LDOPA under continuous hydrothermal conditions. In a second step, NPs were conjugated with PEG (MW = 2000 Da) and to a promising macrocyclic chelator 2,2,2-(2-{[2-(4-isothiocyanatophenyl)-acetamido]methyl}-1,4,7-triazacyclononane-1,4,7-triyl)triacetic acid (*p*-NCS-Bz-MANOTA) to complex $^{64}Cu^{2+}$.[42] MANOTA appeared recently as a very good candidate for copper-64 radiolabeling of antibody fragments.[43] The use of optimized chelators of $^{64}Cu^{2+}$ is crucial because recent studies have shown that Cu(II)−DOTA or 1,8-*N*,*N*′-bis-(carboxymethyl)-1,4,8,11-tetraazacyclotetradecane complexes can undergo metal release in vivo and high accumulation in kidneys and liver.[38−40,44,45] In vivo applications of iron oxide NPs synthesized using a continuous hydrothermal process, functionalized with *p*-NCS-Bz-MANOTA on their surface, have not been reported yet. The resulting bimodal agents showed a significant stability in suspension, no cytotoxicity (in vitro tests) on liver cells (HepG2 cells), and a high contrast on mouse imaging (PET and MRI), highlighting the high potential of these systems for PET/MRI future bimodal applications.

2. RESULTS AND DISCUSSION

2.1. Chemical Characterization of the Functionalized NPs. *2.1.1. Fe_3O_4−LDOPA NPs Synthesized by the Hydrothermal Continuous Process.* The Fe_3O_4−LDOPA NPs synthesized by continuous hydrothermal process have been investigated. The (220), (311), (222), (400), (422), (511), and (440) planes on X-ray diffraction (XRD) pattern[46] (Figure 1a) and A_{1g} transition[47] observed in the Raman

DOI: 10.1021/acsomega.8b03283
ACS Omega 2019, 4, 2637−2648

spectrum (Figure 1b) indicate the cubic inverse spinel structure of magnetite (Fe_3O_4, ICDD: 19-0629). Moreover, in the Raman spectra, maghemite peak at 720 cm^{-1}, which corresponds to a partial oxidation of NPs, is not observed.[48] The lattice parameter determined from the XRD results is a = 8.396 ± 0.003 Å and confirms that Fe_3O_4–LDOPA NPs obtained by this continuous process are nonoxidized. Fe_3O_4–LDOPA NPs exhibit a specific nanoflower structure (Figure 1c) as described in previous reports.[49,50] Briefly, these nanoflowers (small aggregates) are composed of small crystallites ($Ø_{XRD}$ = 14.9 ± 0.3 nm in Figure 1a) organized in a flower-shaped aggregate structure with a mean size of 39 ± 12 nm (Figure 1d).

LDOPA ligands on the surface of NPs are detected by IR spectroscopy. The characteristic vibrations at 1485 cm^{-1} (ν(CC) of the benzene ring),[51] 1590 cm^{-1} (COO^- groups),[52] and 1345 cm^{-1} (ν(CC) and ν(CO))[51] confirm the grafting of LDOPA on the surface of NPs (Figure 2). X-ray photoelectron

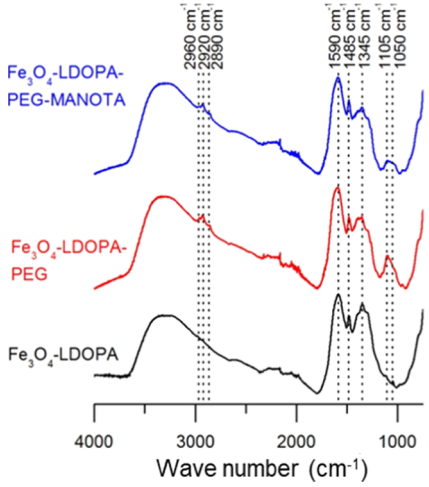

Figure 2. Fourier transform infrared spectra collected from 4000 to 750 cm^{-1} on Fe_3O_4–LDOPA, Fe_3O_4–LDOPA–PEG, and Fe_3O_4–LDOPA–PEG–MANOTA NPs.

spectroscopy (XPS) measurements confirm also the grafting of LDOPA on the surface of iron oxide NPs (Figure 3a). As previously reported,[49] the characteristic peaks of LDOPA are observed on C 1s ($\pi \rightarrow \pi^*$ contribution at 291.4 eV and COOH contribution at 288.3 eV) and on N 1s (NH_2 group, 399.7 eV) levels.

2.1.2. Functionalized Fe_3O_4–LDOPA–PEG and Fe_3O_4–LDOPA–PEG–MANOTA NPs. The different functionalizations were analyzed thanks to thermogravimetric analysis (TGA) to characterize the grafting ratio of PEG and MANOTA at the surface of SPIONs–LDOPA (Figure S1). Mass losses increased as additional organic moieties were added at each successive step of grafting leading to 2.49 LDOPA, 0.07 PEG_{2000}, and 0.04 MANOTA nm^{-2} on the surface of SPIONs. The details of the equation are given in Figure S2. It should be noted that the specific surface area of SPIONs–LDOPA was (S_{BET} = 147 ± 2 m^2 g^{-1}). It was considered that S_{BET} remained the same for all following steps.

XPS measurements indicate an evolution of C 1s, O 1s, and N 1s contribution when samples are modified by PEG and MANOTA, as can been seen in Figure 3. The $\pi \rightarrow \pi^*$ contribution of C 1s peak concerning the Fe_3O_4–LDOPA–PEG NPs disappeared (Figure 3b). It can be explained by the new layer of PEG around the nanoparticle.[53] Moreover, the proportion corresponding to COH/COC/CN groups of C 1s level improves from 30% for the Fe_3O_4–LDOPA NPs to 46% for the Fe_3O_4–LDOPA–PEG NPs as the O–C contribution of O 1s level from 4% for Fe_3O_4–LDOPA NPs to 12% for Fe_3O_4–LDOPA–PEG NPs. These observations are attributed to the large number of COC groups in PEG (MW: 2000 Da). Furthermore, the O^{2-} contribution (structure oxygen from NPs) of O 1s level and COOH contribution of C 1s level decrease for Fe_3O_4–LDOPA–PEG NPs compared to Fe_3O_4–LDOPA. Finally, a shift of binding energies concerning COOH and O–C contributions of Fe_3O_4–LDOPA–PEG NPs compared to Fe_3O_4–LDOPA NPs are observed. These shifts to low binding energy are equal to 0.2 and 0.7 eV (COOH and OC, respectively). The COOH shift indicates a modification of the electronic environment around this group. It is due to the covalent linkage between COOH of LDOPA and NH_2 of MeO–PEG–NH_2. The last shift comes from the large number of COC in PEG. The N 1s contribution is not modified for Fe_3O_4–LDOPA–PEG sample because the NH_2 group of LDOPA is not again modified. These results confirm that a PEG organic shell covers the NPs surface.

Some changes in the Fe_3O_4–LDOPA–PEG–MANOTA sample are also observed (Figure 3c). The COH/COC/CN proportion increases from 46% (Fe_3O_4–LDOPA–PEG NPs) to 55% for (Fe_3O_4–LDOPA–PEG–MANOTA NPs). The COOH contribution also increases from 18% (Fe_3O_4–LDOPA–PEG NPs) to 21% (Fe_3O_4–LDOPA–PEG–MANOTA NPs). These observations come from the large number of COOH groups and CN bonds in MANOTA derivatives. The O–C and O=C–OH/OH proportions concerning the O 1s level increase as well. They increase from 33% (Fe_3O_4–LDOPA–PEG NPs) to 49% (Fe_3O_4–LDOPA–PEG–MANOTA NPs) and from 12% (Fe_3O_4–LDOPA–PEG NPs) to 25% (Fe_3O_4–LDOPA–PEG–MANOTA NPs). It is due to the COOH groups of MANOTA-NCS and confirms the presence of the chelator on the surface of NPs. Moreover, the O^{2-} contribution decreases to 26% for Fe_3O_4–LDOPA–PEG–MANOTA NPs. The COOH contribution of the C 1s level is modified. A shift to high binding energies from 288.1 eV (Fe_3O_4–LDOPA–PEG NPs) to 288.4 eV (Fe_3O_4–LDOPA–PEG–MANOTA NPs) is observed. A shift to low binding energies of the O–C contribution is also highlighted in the O 1s level, showing a decrease from 532.5 eV for Fe_3O_4–LDOPA–PEG NPs to 532.0 eV for Fe_3O_4–LDOPA–PEG–MANOTA NPs This can be explained by the CO groups of MANOTA. Finally, we also observed a modification of the N 1s level: after the conjugation of *p*-NCS-Bz-MANOTA with the NH_2 group of LDOPA, a slight shift to high binding energies is observed. This increase from 399.7 eV (Fe_3O_4–LDOPA–PEG NPs) to 400.0 eV (Fe_3O_4–LDOPA–PEG–MANOTA NPs) can be attributed to the CN contributions of MANOTA cycles, which have similar (cyclic) structure to other polyazamacrocycles for which similar behavior has already been observed in literature.[54] XPS data confirm the grafting of *p*-NCS-Bz-MANOTA on the NPs surface (Fe_3O_4–LDOPA–PEG). These results show that NH_2 and COOH groups of LDOPA (after the continuous hydrothermal synthesis of magnetite NPs) are free and available for grafting other molecules, like in this case PEG and MANOTA, both present on the surface of NPs.

In the IR spectra of Fe_3O_4–LDOPA–PEG and Fe_3O_4–LDOPA–PEG–MANOTA NPs, new vibration bands are

DOI: 10.1021/acsomega.8b03283
ACS Omega 2019, 4, 2637–2648

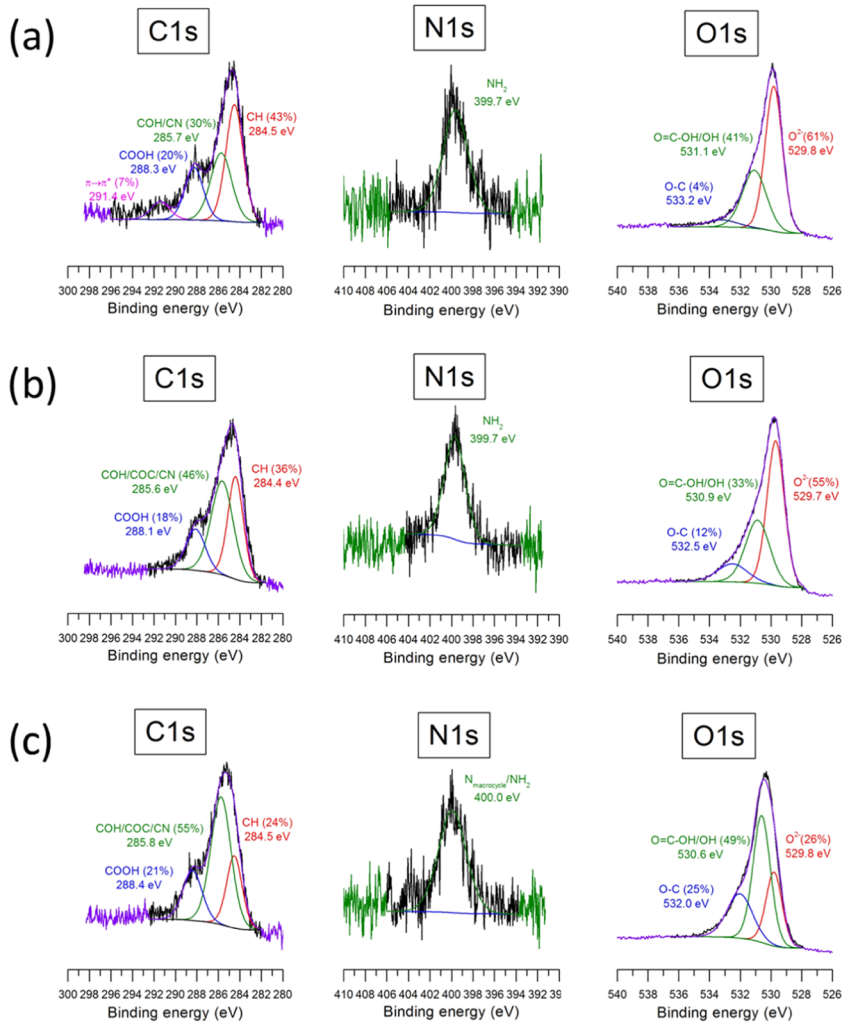

Figure 3. XPS spectra of curve-fitted C 1s, N 1s, and O 1s peaks recorded on (a) Fe_3O_4–LDOPA, (b) Fe_3O_4–LDOPA–PEG, and (c) Fe_3O_4–LDOPA–PEG–MANOTA NPs.

observed compared to that of Fe_3O_4–LDOPA NPs (Figure 2). The vibrations at 2960, 2920, and 2890 cm^{-1} correspond to the asymmetric stretching of CH_2, stretching of CH (CH, symmetric CH_3), and symmetric stretching of CH_2 groups from PEG, respectively.[55] The bands at 1105 and 1050 cm^{-1} are assigned to ether asymmetric stretching.[55,56] The CN, CO, and CC bonds, which compose MANOTA, have the same vibration bands as PEG. The vibration bands of LDOPA are also kept after the grafting of PEG and MANOTA on the surface of NPs. The IR spectroscopy also confirms the grafting of PEG and MANOTA on the NPs' surface.

The ζ-potential measurements (Figure 4) also confirm the grafting of PEG and MANOTA. Fe_3O_4–LDOPA NPs indicate an isoelectric point (IEP) of 2.8 and a ζ-potential of −30 mV at physiological pH (pH = 7.4). A screening of the ζ-potential and a shift of the IEP are observed when the NPs are functionalized by PEG. The IEP and the ζ-potential at physiological pH of Fe_3O_4–LDOPA–PEG NPs are pH 6 and −8 mV, respectively. This screening is due to the presence of PEG on the NPs surface; the absence of charge on this polymer and the presence of covalent bond between the COO^- terminal group of LDOPA and the NH_2 terminal group of MeO–PEG–NH_2 contribute to this effect. This new bond tends to modify and more precisely cancels the electronic

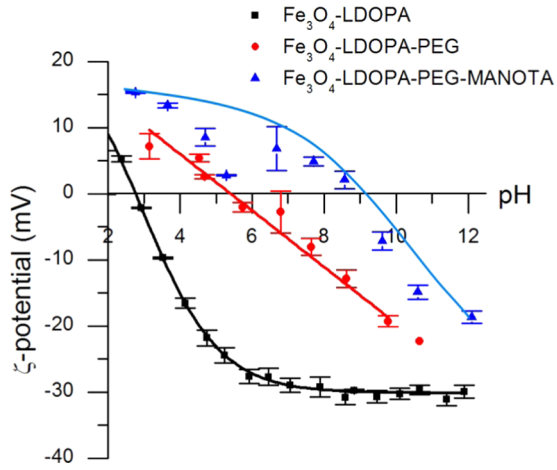

Figure 4. Zetametry of Fe_3O_4–LDOPA, Fe_3O_4–LDOPA–PEG, and Fe_3O_4–LDOPA–PEG–MANOTA NPs.

charges on the COO^- of LDOPA. The latter is corroborated by the new IEP and confirms this grafting. The IEP is shifted to 9.1 (Fe_3O_4–LDOPA–PEG–MANOTA NPs) due to the presence of MANOTA molecules. The ζ-potential range of Fe_3O_4–LDOPA–PEG–MANOTA is the same as that of

DOI: 10.1021/acsomega.8b03283
ACS Omega 2019, 4, 2637−2648

Fe_3O_4–LDOPA–PEG. These results confirm the grafting of MANOTA on the NPs' surface.

IR spectroscopy, XPS, and ζ-potential measurements prove that the NH_2 groups and COO^- of LDOPA of Fe_3O_4–LDOPA NPs, which are synthesized by a hydrothermal synthesis, are available and active for the grafting of PEG and *p*-NCS-Bz-MANOTA.

Dynamic light scattering (DLS) measurements reveal a shift of the hydrodynamic diameter of the NPs in Figure 5. More precisely, a slight increase of the hydrodynamic diameter is observed from 90 ± 2 nm (Fe_3O_4–LDOPA NPs) to 119 ± 6 nm (Fe_3O_4–LDOPA–PEG–MANOTA NPs). The hydrodynamic size does not increase significantly after the grafting of MANOTA. This observation suggests that there is no cross-linking between NPs from carboxyl groups of MANOTA. Grafted PEG molecules participate in the prevention of this phenomenon by a steric effect. The organic layer surrounding the metal oxide increases upon grafting of PEG and MANOTA on the surface of NPs: PEG contributes to a steric hindrance around the NPs. Consequently, this layer extends the hydrodynamic diameter. Moreover, the average hydrodynamic size is under 200 nm, which is efficient for nanoprobe delivery.[57] Moreover, the colloidal stability of SPIONs–LDOPA–PEG_{2000} NPs has been evaluated in several media. The hydrodynamic diameters are as follows: NaCl 10^{-2} M (95 ± 2 nm), phosphate-buffered saline (PBS) 1× (115 ± 4 nm), minimal essential medium (MEM, 106 ± 1 nm), and albumin 60 mg mL^{-1}, 24 h at 37 °C (120 ± 2 nm). We can see that the hydrodynamic size remains almost the same whatever the conditions.

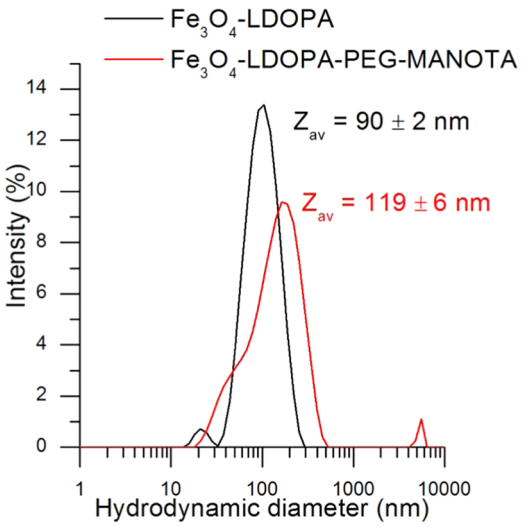

Figure 5. DLS measurements of Fe_3O_4–LDOPA and Fe_3O_4–LDOPA–PEG–MANOTA NPs in PBS (0.1 M).

2.2. In Vitro Cytotoxicity Test. The cytotoxicity of Fe_3O_4–LDOPA–PEG–MANOTA NPs is evaluated on HepG2 liver cells (Figure 6), which are exposed to a wide range of NPs concentrations from 2.34 to 300 $\mu g_{Fe_3O_4}$ mL^{-1}. Positive cells exposed to a toxic agent (sodium dodecyl sulfate 3%) and negative controls (without exposition) are realized. Whatever the NPs concentration, the cell viability is approximately 80–90%, which is not statistically different from the negative control. Indeed, we evaluate with this test a high concentration of NPs (until 300 μg mL^{-1}) compared to those mentioned in the reported literature.[58,59] No dose effect is observed in the present study. The mitochondrial enzymatic activity of HepG2 cells is maintained when they are exposed to the functionalized NPs during 24 h. Thanks to these results, an in vivo evaluation of Fe_3O_4–LDOPA–PEG–MANOTA NPs on animals (mice) was performed.

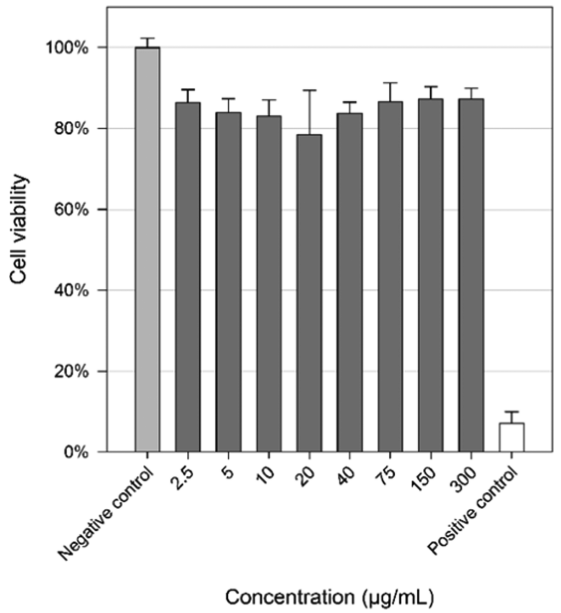

Figure 6. Cytotoxicity of HepG2 cells in the resazurin assay after exposure to different concentrations (μg mL^{-1}) of Fe_3O_4–LDOPA–PEG–MANOTA NPs for 24 h. Results are expressed as mean ± standard deviation (three independent experiments). Statistical difference was checked using a one-way analysis of variance (ANOVA) followed by a Dunnett test ($p < 0.05$).

2.3. In Vivo Evaluation. *2.3.1. Radiolabeling and PET/CT Imaging.* In vivo PET imaging application of Fe_3O_4–LDOPA–PEG–MANOTA NPs on an animal model (mice) was performed to test the stability of the ^{64}Cu–MANOTA complex in a first set of experiments. Fe_3O_4–LDOPA–PEG–MANOTA was radiolabeled with ^{64}Cu with satisfying specific activity (3 MBq μmol_{Fe}^{-1}). Radiolabeling yield was only 60% before purification, which may be explained by complexation of iron ions present in solution, leading to a competition between iron and copper chelation.

An amount of 0.8–1.2 μmol_{Fe} per mouse with an initial activity (at t_0) of 2.5–3.7 MBq per mouse (^{64}Cu) is injected. Then, images are acquired 1 and 24 h after injection (Figure 7). After 1 h, a large uptake of Fe_3O_4–LDOPA–PEG–MANOTA–^{64}Cu NPs is observed in the liver, spleen, and bladder. In addition, a small activity is observed in lungs and digestive system. After 24 h, most of the radioactivity disappeared. Nevertheless, a scale up of the image after 24 h allows to show the low remaining activity in the liver with a weak signal in the spleen and digestive system. Fe_3O_4–LDOPA–PEG–MANOTA–^{64}Cu NPs are progressively eliminated from the body after 24 h.

A biodistribution study of Fe_3O_4–LDOPA–PEG–MANOTA–^{64}Cu NPs was performed to determine the potential of these NPs as a bimodal PET/MRI in vivo probe. First, several blood samples were analyzed (Figure 8). After 1 h, the activity of Fe_3O_4–LDOPA–PEG–MANOTA–^{64}Cu NPs in the bloodstream decreases quickly from ∼8 to ∼2%. As demonstrated in Figure 8, the blood clearance of SPIONs

DOI: 10.1021/acsomega.8b03283
ACS Omega 2019, 4, 2637–2648

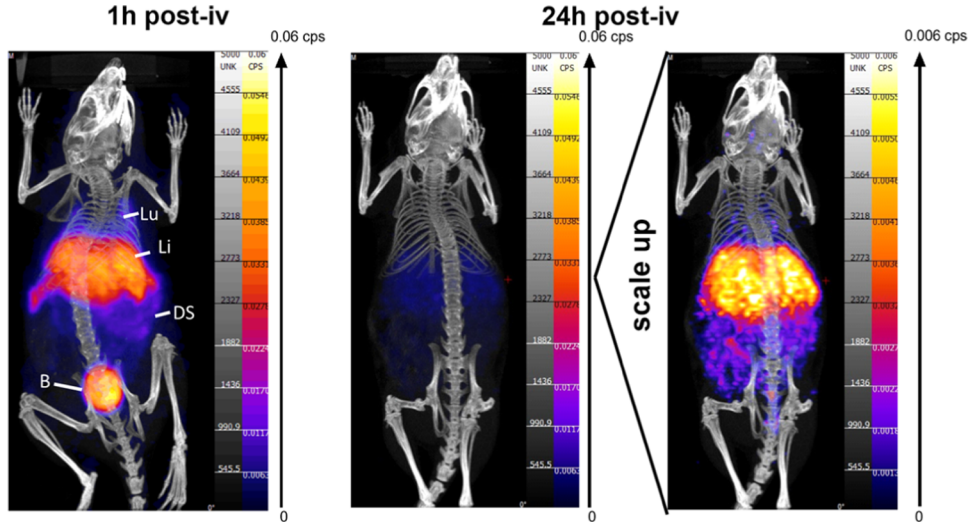

Figure 7. Whole-body PET imaging of Fe_3O_4–LDOPA–PEG–MANOTA–^{64}Cu NPs on mouse 1 and 24 h after injection with a scale up at 24 h. Labels: B = bladder, DS = digestive system, Li = liver, and Lu = lungs.

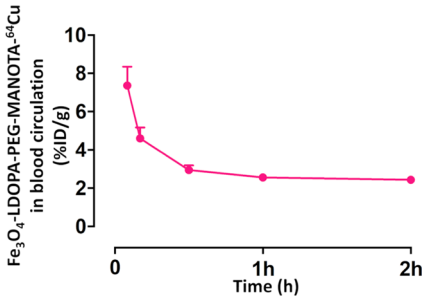

Figure 8. Evaluation of the injected dose (Fe_3O_4–LDOPA–PEG–MANOTA–^{64}Cu) per gram (tissue) in blood circulation on three mice during 2 h following intravenous injection.

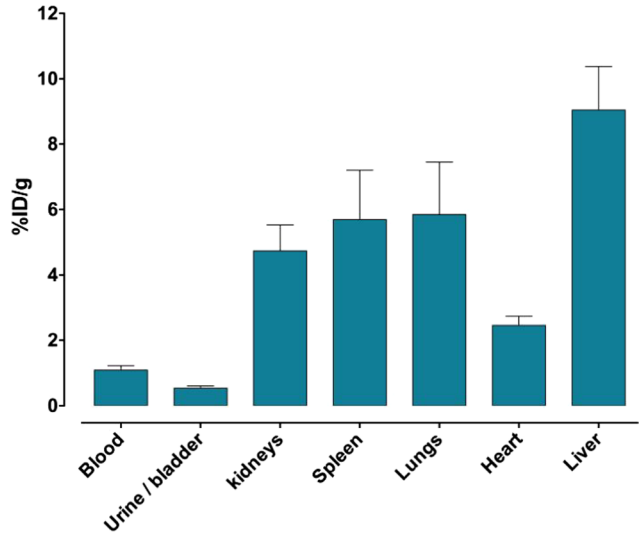

Figure 9. Evaluation of the biodistribution of Fe_3O_4–LDOPA–PEG–MANOTA–^{64}Cu NPs 48 h after intravenous injection in mice. Values represent the mean ± standard deviation of the percentage of the injected dose per gram of tissue in different organs (n = 4).

was fast. This phenomenon is due to the particle charges (+6 mV) and their relatively large size (119 ± 6 nm). Another reason would be their surface coating. Longer circulation half-life has been noted on ^{64}Cu-labeled magnetite NPs[60] (37% of the injected dose remained in blood after 1 h), maybe due to the PEGylated phospholipids coating of these nanoparticles or to smaller hydrodynamic sizes (20.3 ± 1.9 nm).

Then, we observe that the radioactivity is mainly localized in the liver (9% ID g^{-1}), spleen (6% ID g^{-1}), lungs (6% ID g^{-1}), and kidneys (5% ID g^{-1}) with a low activity in the heart (3% ID g^{-1}) after 48 h (Figure 9). These results confirm the PET images (Figure 7). A previous study reveals that a hydrodynamic size of 85 nm also induces a rapid clearance.[36] Moreover, it has been previously reported that positively charged nanoparticles can lead to nonspecific internalization rate and short blood circulation half-life.[61] Nevertheless, after 48 h, a small activity in blood (1% ID g^{-1}) and heart (2% ID g^{-1}) is still detected (Figure 9). This low activity in bloodstream (heart and lungs, both of which are heavily vascularized tissues) shows that NPs followed the pattern of blood retention.[60] Our biodistribution study is in accordance with a previous study with different ^{64}Cu-labeled superparamagnetic iron oxide NPs for PET/MRI imaging (NOTA macrocycle).[33] These observations seem to prove that MANOTA does not desorb from the surface of NPs. By adding the activities obtained by the γ-counting of all organs and carcasses to the data, we determine the remaining activity in the animal at the time of euthanasia. Fifty percent of the injected dose is eliminated after 48 h. These results show that we can deliver high doses in liver and spleen. These bimodal contrast agents can be very interesting for some liver pathologies that lack precision of current imaging procedures, such as infections[62] or cystic lesions,[63] for which multimodal imaging may improve early diagnosis and takeover. Moreover, we show and confirm that MANOTA has a high efficiency to complex ^{64}Cu with good stability as recently reported.[43] Indeed, we have also analyzed, via magnetic susceptibility method (Figure S4), the urine of the injected animals and found some signal demonstrating the presence of SPIONs in the bladder and urine. It is possible that due to the polydispersity of our nanoparticles, the smallest ones could have been excreted in urine, explaining the presence of radioactivity in this organ without ^{64}Cu decomplexation from particle surface during circulation. Thus, we proved that when radioactivity was observed in urine, the presence of SPIONs

DOI: 10.1021/acsomega.8b03283
ACS Omega 2019, 4, 2637–2648

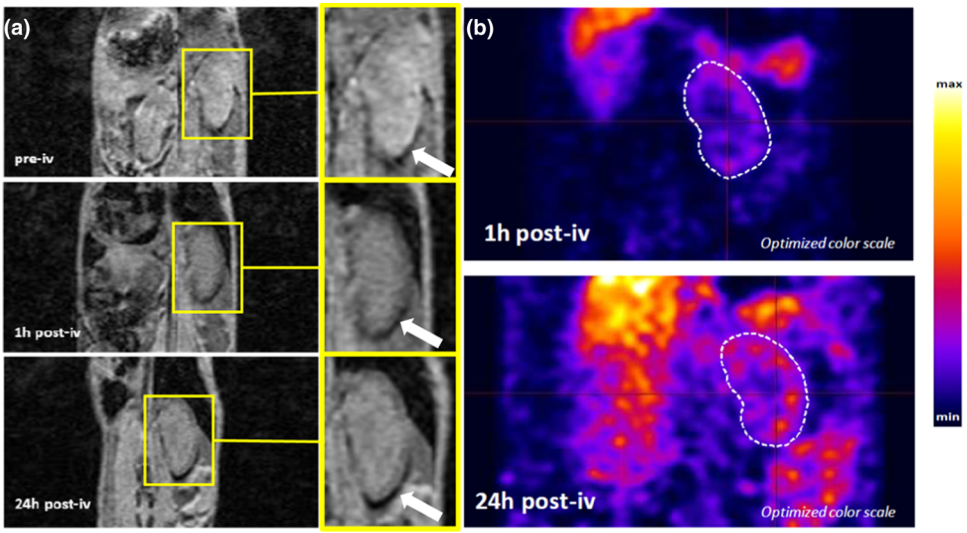

Figure 10. (a) Three-dimensional (3D) T_2*-weighted MR images and (b) PET imaging of renal cortex at different time of injection: before injection (pre-iv) for MRI, after 1 h (1 h post-iv), and 24 h (24 h post-iv) after injection of Fe_3O_4−LDOPA−PEG−MANOTA−^{64}Cu NPs in a mouse.

was also proven, demonstrating that these nanohybrids were excreted intact.

Consequently, the Cu^{64}-radiolabeled Fe_3O_4−LDOPA−PEG−MANOTA NPs are detectable by PET imaging, with a rapid elimination from the body and main metabolism in liver. The fast clearance as well as the imaging capabilities confirm that a novel NP-based PET imaging probe was successfully developed. MANOTA, a recently developed macrocycle, was grafted for the first time and with a high efficiency on the surface of prefunctionalized NPs (Fe_3O_4−LDOPA) synthesized thanks to a continuous hydrothermal process. No previous study reports the grafting and the study of this macrocycle (MANOTA) on magnetite NPs for an in vivo application. For this reason, we decided to further investigate our compounds, and we could carried out a second in vivo set of experiments combining MRI and PET imaging to test the bimodal potential of Fe_3O_4−LDOPA−PEG−MANOTA NPs.

2.3.2. In-Line PET/MRI Imaging. The Fe_3O_4−LDOPA−PEG−MANOTA NPs show a high transverse relaxivity (r_2 = 360 ± 10 mM_{Fe}^{-1} s^{-1}), which confirms that these NPs are an excellent probe for T_2 and T_2*-weighted MRI. We conducted thereby a PET/MRI imaging study, using a new and innovative apparatus, which allows to perform MRI and PET sequentially within the same imaging session without the transfer of mice between each imaging technique. MR signal variation was evaluated in the cortex of the kidneys and the liver for this experience. Three-dimensional (3D) T_2*-weighted MRI images were performed before, 1 and 24 h after injection of the particle suspension and PET imaging was performed after 1 and 24 h. MRI images show a clear negative contrast effect in the renal cortex (outer structure of kidneys) 1 and 24 h after injection compared with images before injection (Figure 10a). The observed signal variations in the kidneys could be distinguished on MRI images as a gradual darkening of the renal cortex signal (Figures 10a). PET imaging (Figure 10b) also shows activity in liver after 1 and 24 h. These observations combined with the previous study confirm that Fe_3O_4−LDOPA−PEG−MANOTA−^{64}Cu NPs have bimodal imaging properties with high transverse relaxation and radioactive property. Moreover, PET studies combined with MRI show that ^{64}Cu is not dissociated from its complex with MANOTA macrocycle grafted on the surface of NPs, which has already been observed for ^{64}Cu−DOTA and TETA complexes.[60,64] Indeed, ^{64}Cu, detected thanks to PET, was localized in the same organs than SPIONs, detected thanks to MRI. Biodistribution data and PET/MRI images show that Fe_3O_4−LDOPA−PEG−MANOTA−^{64}Cu NPs are efficient for liver, kidneys, and spleen evaluation.

3. CONCLUSIONS

In this study, for the first time, we succeeded in grafting PEG and MANOTA chelator on prefunctionalized iron oxide NPs (Fe_3O_4−LDOPA) synthesized under continuous hydrothermal conditions (150 °C and 25 MPa) for bimodal PET/MRI imaging. The characterization of the functionalized NPs (XPS, IR, ζ-potential, and DLS analyses) confirmed that it is possible to graft PEG and MANOTA on COOH and NH_2 groups of LDOPA, respectively. The hydrodynamic size of the NPs under 200 nm is relevant for use as an in vivo contrast agent. The functional groups of LDOPA remain available after the continuous hydrothermal synthesis. Bimodal imaging PET/MRI experiments are encouraging, as these NPs are detectable in both PET and MRI with a high contrast. They highlight an activity in the liver, spleen, lungs, and kidneys with a gradual elimination from the body. NPs showed a high contrast between tissues without NPs and tissues with functionalized NPs. These results are promising and point out the potential benefits of MANOTA-labeled iron oxide nanoparticles as a good candidate for a bimodal PET/MRI tracer. Additionally, a specific targeting may be envisaged with the grafting of proteins on the surface of NPs to develop a diagnostic imaging agent.

4. MATERIALS AND METHODS

4.1. Chemicals. Iron(III) sulfate (97%), ammonium iron(II) sulfate hexahydrate (99%), sodium hydroxide (99%), LDOPA (98%), *N*-hydroxysuccinimide (98%) *N*,*N*-diisopropylethylamine (DIEA) (99.5%), and *N*-(3-dimethylaminopropyl)-*N*′-ethylcarbodiimide hydrochloride were purchased from Sigma-Aldrich. Demineralized water (conductivity,

DOI: 10.1021/acsomega.8b03283
ACS Omega 2019, 4, 2637−2648

σ = 2.2 μS cm^{-1}) was used for the hydrothermal synthesis. Phosphate buffered saline (PBS) 1× solution was purchased from Fisher Bioreagents. Extra dry dimethyl sulfoxide (DMSO > 99.7%) was purchased from Acros. MeO−PEG−NH_2 (molecular weight, MW = 2000 Da) was purchased from Iris Biotech GmbH. 2,2,2-(2-{[2-(4-Isothiocyanatophenyl)-acetamido]methyl}-1,4,7-triazacyclononane-1,4,7-triyl)triacetic acid (*p*-NCS-Bz-MANOTA) was synthesized as previously described.[42] ^{64}Cu copper chloride ($^{64}CuCl_2$, 1 in 0.1 N HCl) was purchased from Arronax (Saint-Herblain, France). The radiolabeling yield and the absence of free ^{64}Cu in the labeled constructs were determined using instant thin layer chromatography impregnated with silica gel (ITLC-SG) strips (Agilent, Santa-Clara, CA).

4.2. Characterization. *4.2.1. Powder X-ray Diffraction (XRD) Characterization.* XRD pattern was collected using a Siemens D5000 diffractometer with Cu Kβ radiation (λ = 1.39222 Å). Scans were acquired over a 2θ range of 20−59° with a step size of 0.03° and a scan speed of 150 s per angle. Diffract-AT software was used for the data analysis (curve fitting). Correction of instrumental broadening was carried out using a standard reference material (Quartz). The mean crystallite size of the samples was calculated using Halder and Wagner method by XRD line-broadening technique.[65] The lattice parameter of the powder was deduced from the XRD line positions using a least-squares refinement method (in-house software taking into account the effect of sample gap).

4.2.2. Transmission Electron Microscopy (TEM) Observations. TEM measurements were performed using a JEOL JEM-2100F microscope operating at 200 kV (point-to-point resolution of 0.19 nm). A diluted suspension of NPs in deionized water was evaporated on a carbon-coated copper grid. The average size of crystallites was calculated by counting 100 individual nanoparticles. The size distribution curves were calculated using a Gaussian fit.

4.2.3. Surface Area Measurements. Specific surface area measurement was performed with a Micromeritics Tristar II apparatus and calculated with the Brunauer−Emmett−Teller (BET) method (S_{BET}) from N_2 gas adsorption. The samples were first outgassed in situ (20 mTorr; 100 °C; 16 h).

4.2.4. ζ-Potential Measurements and Dynamic Light Scattering (DLS) Measurements. ζ-Potential and DLS measurements were carried out with Malvern Zetasizer Nano ZS supplied with DTS Nano V7.12 software. For each ζ-potential measurement, powders were dispersed in 12 mL of NaCl aqueous solution (10^{-2} M). pH titrations were performed using HCl (0.1 M), NaOH (0.1 M), or NaOH (0.01 M) aqueous solutions. The DLS measurements of suspensions were performed at 25 ± 0.1 °C in NaCl (10^{-2} M). The samples were filtered (0.45 μm filter) to remove possible pollutants or large agglomerates. The DLS curves were derived from intensity calculations.

4.2.5. Infrared (IR) Spectroscopy Measurements. IR spectroscopy measurements were performed on ATR mode using Thermofisher Iz10. The IR spectra were collected in the wavenumber range of 4000−750 cm^{-1} with a resolution of 4 cm^{-1}.

4.2.6. X-ray Photoelectron Spectroscopy (XPS) Measurements. XPS measurements were carried out using a PHI 5000 Versaprobe instrument with an Al Kα monochromatic radiation ($E_{K\alpha}$(Al) = 1486.7 eV with a spot size 200 μm in diameter). The powders were pressed on an indium sheet. Data were analyzed with CasaXPS processing and MultiPak software. Neutralization method was employed to minimize the charging effects and the carbon C 1s peak at 284.5 eV was used as the reference. As LDOPA, PEG, and MANOTA are insulators, neutralization process is required. A Shirley background was subtracted and Gauss (70%)−Lorentz (30%) profiles were used. Full width at half-maximum was fixed between 1.5 and 2.4 eV except for the fitted C 1s (π−π*) peak (2.3 eV). The MultiPak software was employed for the quantitative analysis.

4.2.7. Thermogravimetric Analysis (TGA) Measurements. The powders were analyzed using Discovery TGA-TA Instruments with a nitrogen flow rate of 25 mL min^{-1}. A temperature ramp of 5 °C min^{-1} from 25 to 800 °C was employed.

4.2.8. Relaxivity Measurements. The particle transverse relaxivity (r_2 in mM_{Fe}^{-1} s^{-1}) was calculated according to the following method.[66] Water proton transverse relaxation time (T_2) measurements at 3 T were carried out at 298 ± 1 K with a Siemens Magnetom Trio TIM using a commercially available birdcage head coil. Relaxation time measurements were performed on test tubes containing SPIONs in acrylamide gel at different concentrations (0, 1, 3, 5, 7, and 10 μg_{Fe} mL^{-1}). For T_2 determination, a multi-echo spin-echo pulse sequence was used, with a repletion time (TR) of 5000 ms, a matrix of 256 × 204, a FOV of 100 × 80 mm^2, and a slice thickness of 5 mm. Images were acquired at 32 echoes, from a TE of 8 ms to 256 ms with a 8 ms interval. Image analyses were performed using ImageJ (image analysis software developed by NIH). The signal-decay curve was fitted using a nonlinear function with an equation of $S(TE) = A\, e^{(-T_E/T_2)}$, and the relaxivity, r_2 (in mM_{Fe}^{-1} s^{-1}), was determined by fitting the curve of relaxation rate ($1/T_2$) versus the iron concentration in μg_{Fe} mL^{-1}.

4.2.9. Magnetic Susceptibility Measurements (MSM). Magnetic susceptibility measurements were performed on a Bartington MS3 magneto-susceptometer at 300 K. A MS2G monofrequency sensor was used for around 1 mL cells operated at 1.3 kHz. Before every measurement, a control cell with the same media or material without any SPION was measured and subtracted as background.[67] A calibration curve realized with LDOPA−SPIONs was used to determine the quantity of nanoparticles in different media/organs.

4.2.10. In Vivo PET-CT and PET-MR Imaging. All animal studies were conducted in accordance with the legislation on the use of laboratory animals (directive 2010/63/EU) and approved by accredited Ethical committee (C2ea Grand Campus no. 105). Female CD-1 mice (20−25 g, Charles River, France) were used.

In the first set of experiments, PET-CT imaging was performed using BioPET-CT preclinical imaging system (Bioscan). Whole-body CT scan was acquired using the following parameters: 150 μA, 45 kV, 360 projections, and 8 shots/projection. Whole-body 45−60 min static PET image was obtained using 250−700 keV energy window.

In the second set of experiments, a sequential MRS-PET system (MR solutions, U.K.) was used. This system associates a 3T cryogen free magnet MRS 3000 with a clip-on SiPM PET ring. PET (250−700 keV) and MRI acquisitions (scout images followed by a gradient echo sequence—FLASH-3D: TE 5 ms; TR 40 ms; 0.5 mm slice thickness—acquired in the coronal plane) were performed sequentially. Animal respiration was

DOI: 10.1021/acsomega.8b03283
ACS Omega 2019, 4, 2637−2648

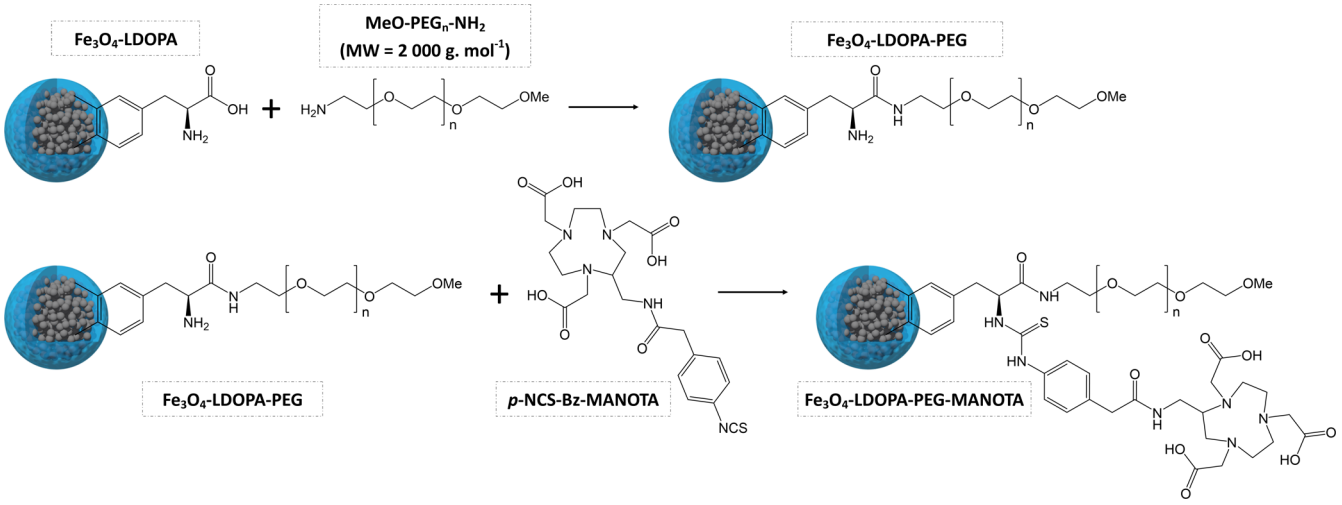

Figure 11. Schematic view of the conjugation chemistry between Fe_3O_4–LDOPA NPs with PEG and *p*-NCS-Bz-MANOTA.

monitored with abdominal pressure sensor and dedicated software (PC Sam, SAII, Stony Brook).

Finally, the PET-CT and PET-MR fusion images were obtained using VivoQuant (Invicro, Boston). Each scan was then visually interpreted.

For biodistribution evaluation, the mice were euthanized, organs were collected and weighed, and radioactivity was measured with a scintillation γ-counter (Cobra 4180, PerkinElmer, Waltham, MA).

4.3. Methods. *4.3.1. Fe_3O_4–LDOPA NPs Synthesis.* The Fe_3O_4–LDOPA NPs were synthesized using a hydrothermal continuous process previously reported.[49] Briefly, at 20 °C, a solution of ferrous and ferric ions (8 and 16 mM, respectively) with a 1:2 molar ratio in aqueous solution (High Pressure Pump 1, HPP 1), 0.33 M of NaOH solution (HPP 2), and preheated demineralized water (HPP 3) was introduced in the counter-current reactor. LDOPA, 24 mM, was added to the metallic salt precursors. The suspension was then quickly cooled to stop the growth of NPs in two steps by the addition of water (HPP 4) at 20 °C and using a cooling bath. The experiment was conducted at 150 °C and 25 MPa in the whole apparatus with a total flow rate of 80 mL min^{-1} (4 × 20 mL min^{-1}). The product was washed by dialysis (Cellu·Sep tubular membranes of 3500 Da) and ultrafiltered (Amicon UltraCell 30 kDa) until the dielectric constant value of demineralized water was obtained (2.2 μS cm^{-1}). Dry powder was obtained by lyophilization for subsequent analysis. A small amount was saved in suspension for DLS and TEM measurements.

4.3.2. Conjugation of Fe_3O_4–LDOPA NPs with PEG. Fe_3O_4–LDOPA NPs, 17.5 mg, were suspended in 5 mL of DMSO. The suspension was placed in a sonic bath for 3 min (30 W) and then using an ultrasonic probe for 10 s (80% of a 400 W Branson Ultrasonic device). EDC, 76.85 mg, and then NHS, 113.92 mg, were added to the suspension and placed in a sonic bath for 10 s (30 W). An orbital shaker was then applied for 15 min. The product was mixed with 100 mg of MeO–PEG–NH_2 (MW: 2000 Da) and 700 μL of DIEA. Finally, the suspension was placed under an orbital shaker for 3 h. The suspension (Fe_3O_4–LDOPA–PEG) was purified by ultrafiltration (Amicon UltraCell 30 kDa). A schematic view of the conjugation chemistry between the Fe_3O_4–LDOPA NPs with PEG is presented in Figure 11.

4.3.3. Conjugation of Fe_3O_4–LDOPA–PEG NPs with p-NCS-Bz-MANOTA. Fe_3O_4–LDOPA–PEG NPs, 10.1 mg, were suspended in 5 mL of DMSO. The suspension was placed in a sonic bath for 3 min and then under an ultrasonic tip for 10 s (80% of a 400 W Branson Ultrasonic device). Seven hundred microliters of DIEA were added. *p*-NCS-Bz-MANOTA, 7.9 mg, were added to the suspension, which was placed under an orbital shaker for 3 h. The final suspension (Fe_3O_4–LDOPA–PEG–MANOTA) was purified by ultrafiltration (Amicon UltraCel 30 kDa). A schematic view of the conjugation chemistry between Fe_3O_4–LDOPA NPs with PEG and *p*-NCS-Bz-MANOTA is presented in Figure 11.

4.4. Radiolabeling of Fe_3O_4–LDOPA–PEG–MANOTA NPs by ^{64}Cu. $^{64}CuCl_2$ (94 μL), 116 MBq, was mixed with an equal volume of 1 M $CH_3CO_2NH_4$ buffer, resulting in a final pH of 5.6. 333 μL of Fe_3O_4–LDOPA–PEG–MANOTA (20 μmol Fe, 52 μL) were then added and the mixture was stirred for 45 min at 37 °C. After incubation, 35 μL of 50 mM ethylenediaminetetraacetic acid (EDTA) in 0.1 M $AcONH_4$ was added to chelate the possibly free copper-64. The resulting ^{64}Cu–EDTA was then removed by ultrafiltration with 30 kDa Amicon Ultra, and the product was diluted in PBS, pH 7.4 prior to injection. ITLC was performed to determine the radiolabeling yield and to assess the absence of free ^{64}Cu. ITLC-SG strip was eluted with sodium citrate 0.1 M, pH 5 and the strip was then analyzed using an AR-2000 radiochromatograph (Eckert & Ziegler, Berlin, Germany) (R_f = 0 for radiolabeled nanoparticles, whereas R_f = 1 for small ^{64}Cu-chelates (i.e., ^{64}Cu–EDTA or ^{64}Cu–AcO)).

4.5. In Vitro Cytotoxicity Study. *4.5.1. Cell Culture.* The human hepatocellular carcinoma cell line HepG2 was obtained from ECACC (European collection of authenticated cell cultures). Routine monitoring has shown the HepG2 cells to be mycoplasma free (MycoAlert PLUS detection kit from Lonza). The cells were grown in a monolayer culture in minimal essential medium (MEM) supplemented with 1% stable glutamine (PAA), 1% nonessential amino acids (PAA), and 10% fetal bovine serum (v/v) (FBS from PAA) in a humidified atmosphere at 37 °C containing 5% CO_2. Continuous cultures were maintained by subculturing flasks every 7 days at 2.10^6 cells/75 cm^2 by trypsination.

4.5.2. Test Plate Preparation. After washing with sterile phosphate buffer saline (PBS), the cells were detached by

DOI: 10.1021/acsomega.8b03283
ACS Omega 2019, 4, 2637–2648

trypsinization (0.05% trypsin/EDTA from Gibco). Twenty-four hours before exposure, HepG2 cells were seeded into 96-well plates (Dutscher, France) in 200 μL of complete culture medium at a final concentration of 1.10^4 cells per well for resazurin assay.

4.5.3. Treatment of HepG2 Cells. The HepG2 cells were grown at 37 °C for 24 h and then exposed to varying concentrations of Fe_3O_4−LDOPA−PEG−MANOTA NPs between 2.34 and 300 μg mL^{-1}. The cytotoxicity was checked at 24 h.

4.5.4. Resazurin Assay. The cell viability was assessed using resazurin assay. This dye is taken up in cells by passive diffusion and reduced in mitochondria. Continued growth maintains a reduced environment and causes the redox indicator to change from oxidized form (Resazurin: non-fluorescent, blue) to reduced form (Resorufin: fluorescent, red). HepG2 cells were seeded into 96-well plate (Dutscher, France) in 200 μL of complete culture medium with 10% FBS at a final concentration of 1.10^4 cells per well. Twenty-four hours after seeding, the medium was removed and the cells were exposed to Fe_3O_4−LDOPA−PEG−MANOTA NPs in complete medium with 0.5% of FBS. The plates were then returned to incubator for 24 h. Medium was removed and replaced with 100 μL resazurin per well and dissolved in MEM 1× without phenol red, yielding a final concentration of 100 μg mL^{-1}. Plates were then placed in the incubator for 3 h and the fluorescence was recorded on a plate reader (Chameleon IV, ScienceTech) (excitation 544 nm, emission 590 nm). The value of the wells containing only MEM and nanoparticles were subtracted from the raw data to take into account the natural fluorescence of Fe_3O_4−LDOPA−PEG−MANOTA. Viability was expressed as %, calculated from fluorescence value emitted by treated cells compared to control (medium or vehicle only), and fixed at 100%. Mean and standard deviations were generated from three independent experiments. The comparison of means was made between different concentrations tested and negative control. Various statistical tests were performed with the GraphPadPrism software. Intergroup comparisons were performed using analysis of variance (ANOVA) followed by Dunnett's test ($p < 0.05$).

4.6. In Vivo Studies. In the first set of experiments, four mice were intravenously injected with 2.5−3 MBq of Fe_3O_4−LDOPA−PEG−MANOTA−^{64}Cu NPs under isoflurane anesthesia. One mouse was imaged by PET-CT at 1 and 24 h after injection. Three other mice were used for blood sampling (one drop harvested at the lateral tail vein, i.e., 20 μL samples) at 5 min, 10 min, 30 min, 1 h, 2 h, and 4 h postinjection times for γ-counting and evaluation of circulating Fe_3O_4−LDOPA−PEG−MANOTA−^{64}Cu NPs levels. At 48 h postinjection time, the four mice were euthanized and organs collected for γ-counting and biodistribution quantification.

In the second set of experiments, after MRI baseline imaging, three mice were intravenously injected with 5−8 MBq of Fe_3O_4−LDOPA−PEG−MANOTA−^{64}Cu NPs under isoflurane anesthesia. The three mice were imaged by PET-MRI at 1 and 24 h postinjection. At 48 h postinjection, the three mice were euthanized and organs collected for γ-counting and biodistribution quantification.

■ ASSOCIATED CONTENT

Supporting Information

The Supporting Information is available free of charge on the ACS Publications website at DOI: 10.1021/acsomega.8b03283.

TGA recorded on Fe_3O_4−LDOPA, Fe_3O_4−LDOPA−PEG, and Fe_3O_4−LDOPA−PEG−MANOTA NPs; theoretical calculation for functionalized-SPIONs rate of grafting; calibration curve of magnetic susceptibility measurements as a function of iron concentration; measurements carried out with SPIONs−LDOPA in water; biodistribution of SPIONs in several organs 1 and 24 h after iv injection; measurements performed using magnetic susceptibility method (PDF)

■ AUTHOR INFORMATION

Corresponding Author

*E-mail: nadine.millot@u-bourgogne.fr.

ORCID

Christine Goze: 0000-0002-3484-3837

Nadine Millot: 0000-0002-0127-3858

Present Address

#(G.T.) NS3E-ISL-CNRS (Nanomatériaux pour les Systèmes Sous Sollicitations Extrèmes) UMR 3208 French−German Research Institute of Saint-Louis, 68300 Saint-Louis, France.

Funding

This work was performed within Pharm'Image, a regional center of excellence in Pharmacoimaging. Support was provided by the French Government through the French National Research Agency (ANR) under the program "Investissements d'Avenir" (ANR-10-EQPX-05-01/IMAPPI Equipex) and the CNRS, the "Université de Bourgogne" and the "Conseil Régional de Bourgogne" through the 3 MIM integrated project ("Marquage de Molécules par les Métaux pour l'Imagerie Médicale"). This work is also part of the project "Pharmacoimagerie et agents théranostiques", funded by the "Université de Bourgogne" and the "Conseil Régional de Bourgogne" through the "Plan d'Actions Régional pour l'Innovation (PARI)" and the European Union through the PO FEDER-FSE Bourgogne 2014/2020 programs.

Notes

The authors declare no competing financial interest.

■ ACKNOWLEDGMENTS

The authors would like to thank Dr. Lucien Saviot for his help in Raman spectroscopy investigations, Dr. Olivier Heintz for XPS analysis, and Dr. Rémi Chassagnon for TEM images.

■ REFERENCES

(1) Wang, Y. X.; Hussain, S. M.; Krestin, G. P. Superparamagnetic Iron Oxide Contrast Agents: Physicochemical Characteristics and Applications in MR Imaging. *Eur. Radiol.* **2001**, *11*, 2319−2331.

(2) Zhang, L.; Dong, W.-F.; Sun, H.-B. Multifunctional Superparamagnetic Iron Oxide Nanoparticles: Design, Synthesis and Biomedical Photonic Applications. *Nanoscale* **2013**, *5*, 7664−7684.

(3) Nigam, S.; Barick, K. C.; Bahadur, D. Development of Citrate-Stabilized Fe_3O_4 Nanoparticles: Conjugation and Release of Doxorubicin for Therapeutic Applications. *J. Magn. Magn. Mater.* **2011**, *323*, 237−243.

(4) Gao, J.; Gu, H.; Xu, B. Multifunctional Magnetic Nanoparticles: Design, Synthesis, and Biomedical Applications. *Acc. Chem. Res.* **2009**, *42*, 1097−1107.

DOI: 10.1021/acsomega.8b03283
ACS Omega 2019, 4, 2637−2648

(5) Shah, N. J.; Oros-Peusquens, A.-M.; Arrubla, J.; Zhang, K.; Warbrick, T.; Mauler, J.; Vahedipour, K.; Romanzetti, S.; Felder, J.; Celik, A.; et al. Advances in Multimodal Neuroimaging: Hybrid MR-PET and MR-PET-EEG at 3 T and 9.4 T. *J. Magn. Reson.* **2013**, *229*, 101−115.
(6) Patel, D.; Kell, A.; Simard, B.; Xiang, B.; Lin, H. Y.; Tian, G. The Cell Labeling Efficacy, Cytotoxicity and Relaxivity of Copper-Activated MRI/PET Imaging Contrast Agents. *Biomaterials* **2011**, *32*, 1167−1176.
(7) Lee, D.-E.; Koo, H.; Sun, I.-C.; Ryu, J. H.; Kim, K.; Kwon, I. C. Multifunctional Nanoparticles for Multimodal Imaging and Theragnosis. *Chem. Soc. Rev.* **2012**, *41*, 2656−2672.
(8) de Rosales, R. T. M. Potential Clinical Applications of Bimodal PET-MRI or SPECT-MRI Agents. *J. Labelled Compd. Radiopharm.* **2014**, *57*, 298−303.
(9) Thomas, R.; Park, I.-K.; Jeong, Y. Y. Magnetic Iron Oxide Nanoparticles for Multimodal Imaging and Therapy of Cancer. *Int. J. Mol. Sci.* **2013**, *14*, 15910−15930.
(10) Huang, W.-Y.; Davis, J. J. Multimodality and Nanoparticles in Medical Imaging. *Dalton Trans.* **2011**, *40*, 6087−6103.
(11) Yang, F.; Li, Y.; Chen, Z.; Zhang, Y.; Wu, J.; Gu, N. Superparamagnetic Iron Oxide Nanoparticle-Embedded Encapsulated Microbubbles as Dual Contrast Agents of Magnetic Resonance and Ultrasound Imaging. *Biomaterials* **2009**, *30*, 3882−3890.
(12) Carril, M.; Fernández, I.; Rodríguez, J.; García, I.; Penadés, S. Gold-Coated Iron Oxide Glyconanoparticles for MRI, CT, and US Multimodal Imaging. *Part. Part. Syst. Charact.* **2014**, *31*, 81−87.
(13) Xie, J.; Chen, K.; Huang, J.; Lee, S.; Wang, J.; Gao, J.; Li, X.; Chen, X. PET/NIRF/MRI Triple Functional Iron Oxide Nanoparticles. *Biomaterials* **2010**, *31*, 3016−3022.
(14) Cheraghipour, E.; Tamaddon, A. M.; Javadpour, S.; Bruce, I. J. PEG Conjugated Citrate-Capped Magnetite Nanoparticles for Biomedical Applications. *J. Magn. Magn. Mater.* **2013**, *328*, 91−95.
(15) Liu, Y.; Li, Y.; Li, X.-M.; He, T. Kinetics of (3-Aminopropyl)-Triethoxylsilane (APTES) Silanization of Superparamagnetic Iron Oxide Nanoparticles. *Langmuir* **2013**, *29*, 15275−15282.
(16) Maurizi, L.; Papa, A.-L.; Dumont, L.; Bouyer, F.; Walker, P.; Vandroux, D.; Millot, N. Influence of Surface Charge and Polymer Coating on Internalization and Biodistribution of Polyethylene Glycol-Modified Iron Oxide Nanoparticles. *J. Biomed. Nanotechnol.* **2015**, *11*, 126−136.
(17) Chung, H. J.; Lee, H.; Bae, K. H.; Lee, Y.; Park, J.; Cho, S.-W.; Hwang, J. Y.; Park, H.; Langer, R.; Anderson, D.; et al. Facile Synthetic Route for Surface-Functionalized Magnetic Nanoparticles: Cell Labeling and Magnetic Resonance Imaging Studies. *ACS Nano* **2011**, *5*, 4329−4336.
(18) Na, H. B.; Palui, G.; Rosenberg, J. T.; Ji, X.; Grant, S. C.; Mattoussi, H. Multidentate Catechol-Based Polyethylene Glycol Oligomers Provide Enhanced Stability and Biocompatibility to Iron Oxide Nanoparticles. *ACS Nano* **2012**, *6*, 389−399.
(19) Lee, H.; Yu, M. K.; Park, S.; Moon, S.; Min, J. J.; Jeong, Y. Y.; Kang, H.-W.; Jon, S. Thermally Cross-Linked Superparamagnetic Iron Oxide Nanoparticles: Synthesis and Application as a Dual Imaging Probe for Cancer in Vivo. *J. Am. Chem. Soc.* **2007**, *129*, 12739−12745.
(20) Panja, S.; Saha, B.; Ghosh, S. K.; Chattopadhyay, S. Synthesis of Novel Four Armed PE-PCL Grafted Superparamagnetic and Biocompatible Nanoparticles. *Langmuir* **2013**, *29*, 12530−12540.
(21) Sandiford, L.; Phinikaridou, A.; Protti, A.; Meszaros, L. K.; Cui, X.; Yan, Y.; Frodsham, G.; Williamson, P. A.; Gaddum, N.; Botnar, R. M.; et al. Bisphosphonate-Anchored PEGylation and Radiolabeling of Superparamagnetic Iron Oxide: Long-Circulating Nanoparticles for in Vivo Multimodal (T_1 MRI-SPECT) Imaging. *ACS Nano* **2013**, *7*, 500−512.
(22) Bae, K. H.; Kim, Y. B.; Lee, Y.; Hwang, J.; Park, H.; Park, T. G. Bioinspired Synthesis and Characterization of Gadolinium-Labeled Magnetite Nanoparticles for Dual Contrast T_1- and T_2-Weighted Magnetic Resonance Imaging. *Bioconjugate Chem.* **2010**, *21*, 505−512.
(23) Bae, K. H.; Park, M.; Do, M. J.; Lee, N.; Ryu, J. H.; Kim, G. W.; Kim, C.; Park, T. G.; Hyeon, T. Chitosan Oligosaccharide-Stabilized Ferrimagnetic Iron Oxide Nanocubes for Magnetically Modulated Cancer Hyperthermia. *ACS Nano* **2012**, *6*, 5266−5273.
(24) Lee, N.; Hummer, D. R.; Sverjensky, D. A.; Rajh, T.; Hazen, R. M.; Steele, A.; Cody, G. D. Speciation of L-DOPA on Nanorutile as a Function of pH and Surface Coverage Using Surface-Enhanced Raman Spectroscopy (SERS). *Langmuir* **2012**, *28*, 17322−17330.
(25) Amstad, E.; Gillich, T.; Bilecka, I.; Textor, M.; Reimhult, E. Ultrastable Iron Oxide Nanoparticle Colloidal Suspensions Using Dispersants with Catechol-Derived Anchor Groups. *Nano Lett.* **2009**, *9*, 4042−4048.
(26) Zirbs, R.; Lassenberger, A.; Vonderhaid, I.; Kurzhals, S.; Reimhult, E. Melt-Grafting for the Synthesis of Core-Shell Nanoparticles with Ultra-High Dispersant Density. *Nanoscale* **2015**, *7*, 11216−11225.
(27) Xie, J.; Xu, C.; Kohler, N.; Hou, Y.; Sun, S. Controlled PEGylation of Monodisperse Fe_3O_4 Nanoparticles for Reduced Non-Specific Uptake by Macrophage Cells. *Adv. Mater.* **2007**, *19*, 3163−3166.
(28) Xie, J.; Xu, C. J.; Xu, Z. H.; Hou, Y. L.; Young, K. L. L.; Wang, S. X.; Pourmand, N.; Sun, S. H. Linking Hydrophilic Macromolecules to Monodisperse Magnetite (Fe_3O_4) Nanoparticles via Trichloro-s-Triazine (Vol 18, Pg 5401, 2006). *Chem. Mater.* **2007**, *19*, 1202.
(29) Yuen, A. K. L.; Hutton, G. A.; Masters, A. F.; Maschmeyer, T. The Interplay of Catechol Ligands with Nanoparticulate Iron Oxides. *Dalton Trans.* **2012**, *41*, 2545−2559.
(30) Price, E. W.; Orvig, C. Matching Chelators to Radiometals for Radiopharmaceuticals. *Chem. Soc. Rev.* **2014**, *43*, 260−290.
(31) Torres Martin de Rosales, R.; Tavaré, R.; Paul, R. L.; Jauregui-Osoro, M.; Protti, A.; Glaria, A.; Varma, G.; Szanda, I.; Blower, P. J. Synthesis of ^{64}CuII−Bis(Dithiocarbamatebisphosphonate) and Its Conjugation with Superparamagnetic Iron Oxide Nanoparticles: In Vivo Evaluation as Dual-Modality PET−MRI Agent. *Angew. Chem., Int. Ed.* **2011**, *50*, 5509−5513.
(32) Torres Martin de Rosales, R.; Tavaré, R.; Glaria, A.; Varma, G.; Protti, A.; Blower, P. J. ^{99m}Tc-Bisphosphonate-Iron Oxide Nanoparticle Conjugates for Dual-Modality Biomedical Imaging. *Bioconjugate Chem.* **2011**, *22*, 455−465.
(33) Yang, X.; Hong, H.; Grailer, J. J.; Rowland, I. J.; Javadi, A.; Hurley, S. A.; Xiao, Y.; Yang, Y.; Zhang, Y.; Nickles, R. J.; et al. CRGD-Functionalized, DOX-Conjugated, and ^{64}Cu-Labeled Superparamagnetic Iron Oxide Nanoparticles for Targeted Anticancer Drug Delivery and PET/MR Imaging. *Biomaterials* **2011**, *32*, 4151−4160.
(34) Lee, H.-Y.; Li, Z.; Chen, K.; Hsu, A. R.; Xu, C.; Xie, J.; Sun, S.; Chen, X. PET/MRI Dual-Modality Tumor Imaging Using Arginine-Glycine-Aspartic (RGD)-Conjugated Radiolabeled Iron Oxide Nanoparticles. *J. Nucl. Med.* **2008**, *49*, 1371−1379.
(35) Pham, T. N.; Lengkeek, N. A.; Greguric, I.; Kim, B. J.; Pellegrini, P. A.; Bickley, S. A.; Tanudji, M. R.; Jones, S. K.; Hawkett, B. S.; Pham, B. T. Tunable and Noncytotoxic PET/SPECT-MRI Multimodality Imaging Probes Using Colloidally Stable Ligand-Free Superparamagnetic Iron Oxide Nanoparticles. *Int. J. Nanomed.* **2017**, *12*, 899−909.
(36) Nosrati, S.; Shanehsazzadeh, S.; Yousefnia, H.; Gholami, A.; Grüttner, C.; Jalilian, A. R.; Hosseini, R. H.; Lahooti, A. Biodistribution Evaluation of ^{166}Ho−DTPA−SPION in Normal Rats. *J. Radioanal. Nucl. Chem.* **2016**, *307*, 1559−1566.
(37) Wang, H.; Li, D.; Liu, S.; Liu, R.; Yuan, H.; Krasnoperov, V.; Shan, H.; Conti, P. S.; Gill, P. S.; Li, Z. Small-Animal PET Imaging of Pancreatic Cancer Xenografts Using a ^{64}Cu-Labeled Monoclonal Antibody, MAb159. *J. Nucl. Med.* **2015**, *56*, 908−913.
(38) Boswell, C. A.; Sun, X.; Niu, W.; Weisman, G. R.; Wong, E. H.; Rheingold, A. L.; Anderson, C. J. Comparative in Vivo Stability of Copper-64-Labeled Cross-Bridged and Conventional Tetraazamacrocyclic Complexes. *J. Med. Chem.* **2004**, *47*, 1465−1474.
(39) Chen, K.; Sun, X.; Niu, G.; Ma, Y.; Yap, L.-P.; Hui, X.; Wu, K.; Fan, D.; Conti, P. S.; Chen, X. Evaluation of ^{64}Cu Labeled GX1: A Phage Display Peptide Probe for PET Imaging of Tumor Vasculature. *Mol. Imaging Biol.* **2012**, *14*, 96−105.

DOI: 10.1021/acsomega.8b03283
ACS Omega 2019, 4, 2637−2648

(40) Dumont, R. A.; Deininger, F.; Haubner, R.; Maecke, H. R.; Weber, W. A.; Fani, M. Novel (64)Cu- and (68)Ga-Labeled RGD Conjugates Show Improved PET Imaging of $\alpha v\beta_3$ Integrin Expression and Facile Radiosynthesis. *J. Nucl. Med.* **2011**, *52*, 1276−1284.
(41) Oxboel, J.; Schjoeth-Eskesen, C.; El-Ali, H. H.; Madsen, J.; Kjaer, A. ^{64}Cu-NODAGA-c(RGDyK) Is a Promising New Angiogenesis PET Tracer: Correlation between Tumor Uptake and Integrin $\alpha v\beta_3$ Expression in Human Neuroendocrine Tumor Xenografts. *Int. J. Mol. Imaging* **2012**, *2012*, 1−11.
(42) Désogère, P.; Rousselin, Y.; Poty, S.; Bernhard, C.; Goze, C.; Boschetti, F.; Denat, F. Efficient Synthesis of 1,4,7-Triazacyclononane and 1,4,7-Triazacyclononane-Based Bifunctional Chelators for Bioconjugation. *Eur. J. Org. Chem.* **2014**, *2014*, 7831−7838.
(43) Moreau, M.; Poty, S.; Vrigneaud, J.-M.; Walker, P.; Guillemin, M.; Raguin, O.; Oudot, A.; Bernhard, C.; Goze, C.; Boschetti, F.; et al. MANOTA: A Promising Bifunctional Chelating Agent for Copper-64 ImmunoPET. *Dalton Trans.* **2017**, *46*, 14659−14668.
(44) Roosenburg, S.; Laverman, P.; Joosten, L.; Cooper, M. S.; Kolenc-Peitl, P. K.; Foster, J. M.; Hudson, C.; Leyton, J.; Burnet, J.; Oyen, W. J. G.; et al. PET and SPECT Imaging of a Radiolabeled Minigastrin Analogue Conjugated with DOTA, NOTA, and NODAGA and Labeled with ^{64}Cu, ^{68}Ga, and ^{111}In. *Mol. Pharm.* **2014**, *11*, 3930−3937.
(45) Hausner, S. H.; Kukis, D. L.; Gagnon, M. K. J.; Stanecki, C. E.; Ferdani, R.; Marshall, J. F.; Anderson, C. J.; Sutcliffe, J. L. Evaluation of [^{64}Cu]Cu-DOTA and [^{64}Cu]Cu-CB-TE2A Chelates for Targeted Positron Emission Tomography with an $\alpha v\beta_6$-Specific Peptide. *Mol. Imaging* **2009**, *8*, 111−121.
(46) Millot, N.; Begin-Colin, S.; Perriat, P.; Le Caër, G. Structure, Cation Distribution, and Properties of Nanocrystalline Titanomagnetites Obtained by Mechanosynthesis: Comparison with Soft Chemistry. *J. Solid State Chem.* **1998**, *139*, 66−78.
(47) Maurizi, L.; Bouyer, F.; Paris, J.; Demoisson, F.; Saviot, L.; Millot, N. One Step Continuous Hydrothermal Synthesis of Very Fine Stabilized Superparamagnetic Nanoparticles of Magnetite. *Chem. Commun.* **2011**, *47*, 11706−11708.
(48) Shebanova, O. N.; Lazor, P. Raman Spectroscopic Study of Magnetite ($FeFe_2O_4$): A New Assignment for the Vibrational Spectrum. *J. Solid State Chem.* **2003**, *174*, 424−430.
(49) Thomas, G.; Demoisson, F.; Heintz, O.; Geoffroy, N.; Saviot, L.; Millot, N. Functionalized Fe_3O_4 Nanoparticles: Influence of Ligand Addition Sequence and pH during Their Continuous Hydrothermal Synthesis. *RSC Adv.* **2015**, *5*, 78614−78624.
(50) Thomas, G.; Demoisson, F.; Chassagnon, R.; Popova, E.; Millot, N. One-Step Continuous Synthesis of Functionalized Magnetite Nanoflowers. *Nanotechnology* **2016**, *27*, No. 135604.
(51) Gulley-Stahl, H.; Hogan, P. A.; Schmidt, W. L.; Wall, S. J.; Buhrlage, A.; Bullen, H. A. Surface Complexation of Catechol to Metal Oxides: An ATR-FTIR, Adsorption, and Dissolution Study. *Environ. Sci. Technol.* **2010**, *44*, 4116−4121.
(52) Socrates, G. *Infrared and Raman Characteristic Group Frequencies: Tables and Charts*, 3rd ed.; Wiley: Chichester, 2010.
(53) Perriat, P.; Fries, E.; Millot, N.; Domenichini, B. XPS and EELS Investigations of Chemical Homogeneity in Nanometer Scaled Ti-Ferrites Obtained by Soft Chemistry. *Solid State Ionics* **1999**, *117*, 175−184.
(54) Jasmin, J.-P.; Ouhenia-Ouadahi, K.; Miserque, F.; Dumas, E.; Cannizzo, C.; Chaussé, A. Straightforward Grafting Approach for Cyclam-Functionalized Screen-Printed Electrodes for Selective Cu(II) Determination. *Electrochim. Acta* **2016**, *200*, 115−122.
(55) Wang, D. K.; Varanasi, S.; Fredericks, P. M.; Hill, D. J. T.; Symons, A. L.; Whittaker, A. K.; Rasoul, F. FT-IR Characterization and Hydrolysis of PLA-PEG-PLA Based Copolyester Hydrogels with Short PLA Segments and a Cytocompatibility Study. *J. Polym. Sci., Part A: Polym. Chem.* **2013**, *51*, 5163−5176.
(56) Coates, J. Interpretation of Infrared Spectra, A Practical Approach. In *Encyclopedia of Analytical Chemistry*; American Cancer Society, 2006.
(57) Kobayashi, H.; Watanabe, R.; Choyke, P. L. Improving Conventional Enhanced Permeability and Retention (EPR) Effects; What Is the Appropriate Target? *Theranostics* **2013**, *4*, 81−89.
(58) Bahadar, H.; Maqbool, F.; Niaz, K.; Abdollahi, M. Toxicity of Nanoparticles and an Overview of Current Experimental Models. *Iran. Biomed. J.* **2016**, *20*, 1−11.
(59) Sruthi, S.; Maurizi, L.; Nury, T.; Sallem, F.; Boudon, J.; Riedinger, J. M.; Millot, N.; Bouyer, F.; Lizard, G. Cellular Interactions of Functionalized Superparamagnetic Iron Oxide Nanoparticles on Oligodendrocytes without Detrimental Side Effects: Cell Death Induction, Oxidative Stress and Inflammation. *Colloids Surf., B* **2018**, *170*, 454−462.
(60) Glaus, C.; Rossin, R.; Welch, M. J.; Bao, G. In Vivo Evaluation of 64Cu-Labeled Magnetic Nanoparticles as a Dual-Modality PET/MR Imaging Agent. *Bioconjugate Chem.* **2010**, *21*, 715−722.
(61) Alexis, F.; Pridgen, E.; Molnar, L. K.; Farokhzad, O. C. Factors Affecting the Clearance and Biodistribution of Polymeric Nanoparticles. *Mol. Pharm.* **2008**, *5*, 505−515.
(62) Ho, A. K.; Girgis, S.; Low, G. Uncommon Liver Lesions with Multimodality Imaging and Pathology Correlation. *Clin. Radiol.* **2018**, *73*, 191−204.
(63) Bächler, P.; Baladron, M. J.; Menias, C.; Beddings, I.; Loch, R.; Zalaquett, E.; Vargas, M.; Connolly, S.; Bhalla, S.; Huete, Á. Multimodality Imaging of Liver Infections: Differential Diagnosis and Potential Pitfalls. *RadioGraphics* **2016**, *36*, 1001−1023.
(64) Bass, L. A.; Wang, M.; Welch, M. J.; Anderson, C. J. In Vivo Transchelation of Copper-64 from TETA-Octreotide to Superoxide Dismutase in Rat Liver. *Bioconjugate Chem.* **2000**, *11*, 527−532.
(65) Langford, J. I. *National Institute of Standards and Technology Special Publication 846*, 1992; p 145.
(66) Papa, A.-L.; Maurizi, L.; Vandroux, D.; Walker, P.; Millot, N. Synthesis of Titanate Nanotubes Directly Coated with USPIO in Hydrothermal Conditions: A New Detectable Nanocarrier. *J. Phys. Chem. C* **2011**, *115*, 19012−19017.
(67) Maurizi, L.; Sakulkhu, U.; Gramoun, A.; Vallee, J.-P.; Hofmann, H. A Fast and Reproducible Method to Quantify Magnetic Nanoparticle Biodistribution. *Analyst* **2014**, *139*, 1184−1191.

DOI: 10.1021/acsomega.8b03283
ACS Omega 2019, 4, 2637−2648